Editors' Suggestion

Strain-Induced Asymmetric Line Segregation at Faceted Si Grain Boundaries

Christian H. Liebscher,[1,*] Andreas Stoffers,[1] Masud Alam,[1] Liverios Lymperakis,[1]
Oana Cojocaru-Mirédin,[2] Baptiste Gault,[1] Jörg Neugebauer,[1] Gerhard Dehm,[1] Christina Scheu,[1] and Dierk Raabe[1]
[1]*Max-Planck-Institut für Eisenforschung GmbH, 40237 Düsseldorf, Germany*
[2]*Institute of Physics (IA), RWTH Aachen University, Sommerfeldstraße 14, 52056 Aachen, Germany*

(Received 3 April 2018; published 6 July 2018)

The unique combination of atomic-scale composition measurements, employing atom probe tomography, atomic structure determination with picometer resolution by aberration-corrected scanning transmission electron microscopy, and atomistic simulations reveals site-specific linear segregation features at grain boundary facet junctions. More specific, an asymmetric line segregation along one particular type of facet junction core, instead of a homogeneous decoration of the facet planes, is observed. Molecular-statics calculations show that this segregation pattern is a consequence of the interplay between the asymmetric core structure and its corresponding local strain state. Our results contrast with the classical view of a homogeneous decoration of the facet planes and evidence a complex segregation patterning.

DOI: 10.1103/PhysRevLett.121.015702

Grain boundaries (GB) are one of the most prominent defects in materials influencing many of their properties [1]. In materials containing more than one element, grain boundaries are usually decorated by solutes, an effect that alters their properties substantially. In the past decades, atomic resolution microscopy techniques have provided new insights into the formation of regular segregation patterns at grain boundaries in metallic and oxide materials [2–6]. These observations go beyond the classical thermodynamic description of interfacial segregation and provide a connection between the structural complexity of the interface and the atomistic arrangement of solutes and impurities segregated to it [7]. In McLean type segregation it is assumed that monolayer or submonolayer coverage of a grain boundary is occurring without any structural change and atomic interactions of the solute atoms [8]. It has recently been established that grain boundaries can not only be structurally and chemically different from bulk phases but also transform between different states, termed complexions or interphase phases [9–12]. Their phase behavior can have a dramatic impact on materials properties as observed by the formation of bi- or even trilayers of solutes at interfaces [11,13]. Typically, these atomic scale segregation patterns are established at planar interfaces but in real materials grain boundaries often possess complex 3D topologies, consisting of a sequence of small facets with alternating local plane normal as drawn in Fig. 1(a), each with a specific atomic arrangement [14–16]. Faceting transitions at grain boundaries are commonly observed in a multitude of material systems impacting their properties such as grain boundary mobility, which is a crucial parameter for material processing [17–19]. Recent atomistic investigations emphasize the impact of facet junctions on the evolution of the overall facet morphology, adding another level of complexity to these interfaces [16]. However, a direct link between the segregation behavior and the complex topology of faceted boundaries is still missing.

To advance our understanding of the interplay between interface structure and composition at the highest possible precision, we performed a systematic structural and compositional analysis of faceted GBs in multicrystalline silicon (mc-Si) by correlating atom probe tomography (APT) and aberration-corrected high angle annular dark-field scanning transmission electron microscopy (HAADF-STEM) [20]. The experimental observations are completed by atomistic calculations combining density functional theory (DFT) with modified embedded atom method (MEAM) potentials, thereby providing a complete picture of segregation at topologically complex interfaces. The majority of large-angle grain boundaries in mc-Si are $\sum 3$, $\sum 9$, and $\sum 27$ coincident-site lattice (CSL) tilt boundaries with $\langle 110 \rangle$ tilt axis (Fig. S1 [21]). Details on the mc-Si material and elemental concentrations are described in Ref. [26]. Recently, it was established that impurity elements tend to segregate to low- and high-angle GBs in mono-like and mc-Si [27,28]. However, these boundaries are often observed to dissociate into low-energy, near CSL facets and are thus an ideal template basis to study segregation effects at faceted interfaces [29].

In this study we show that solute segregation occurs at the linear intersections or junctions of sequential GB facets and not at the averaged planar structure of the GB or at the facets themselves as illustrated in the schematic of Fig. 1(a). Only one particular type of facet junction that is embedded between coherent and incoherent grain boundary segments is found to be a preferred segregation site for carbon (C), iron (Fe), and nitrogen (N). This leads to an

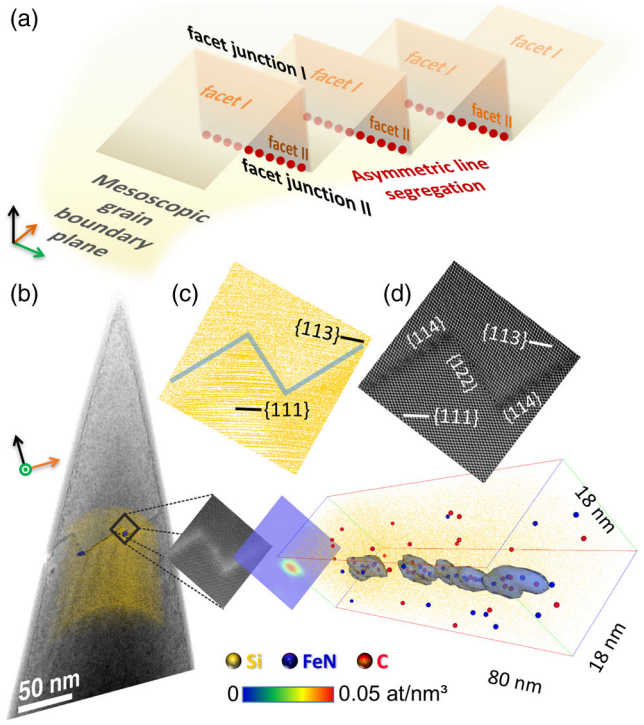

FIG. 1. Atomic structure and chemistry of a faceted $\sum 9$ tilt grain boundary analyzed on a single specimen. (a) Schematic illustration of the faceted interface with asymmetric line segregation. (b) Overview ABF-STEM image of an APT/TEM specimen resolving the faceted structure of the grain boundary superimposed by APT reconstruction. Extended magnification of the highlighted area showing a strain sensitive LAADF-STEM micrograph, a 2D density map of impurities, and a 3D atom map. (c) Corresponding projection of 3D atom map with reconstructed lattice planes and GB topology. (d) High resolution HAADF-STEM image resolving the atomic structure in the vicinity of the right-hand GB junction.

asymmetric segregation pattern with respect to the facet structure, where solutes form segregation lines at facet junctions. Atomistic calculations establish a link between the local core structure and strain state of individual facet junctions and their related segregation tendency. The linear nature of this segregation phenomenon is in complete contrast to the generally assumed and often observed planar segregation pattern formation at grain boundaries [2–6].

The atomic structure of a faceted $\sum 9$ GB was directly obtained in an APT specimen via preceding STEM imaging subsequently followed by APT characterization to extract the 3D elemental distribution of the same feature. The side-projection of the reconstructed APT data set is superimposed onto the annular bright-field (ABF) STEM image of the needle shaped specimen shown in Fig. 1(b). The common $\langle 110 \rangle$ tilt axis of both grains and the retained structural elements in the APT data are used to precisely co-align the tomographic reconstruction and the electron micrograph [30]. As seen in the STEM images, the faceted grain boundary is composed of long incoherent $\sum 9\{114\}$ segments (~48 nm) and short coherent $\sum 9\{122\}$ interfaces (10–20 nm). The facet segments are linked by two types of linear facet junctions (I) and (II) shown schematically in Fig. 1(a). A set of isodensity surfaces encompassing regions containing over 0.15 C + FeN at/nm^3 (blue) is superimposed onto the atom map to highlight the location of high impurity concentrations of C, Fe, and N. These segregation lines have a spacing of ~49 nm that perfectly corresponds to the separation distance of the facet junctions (II). The scatter of solute atoms perpendicular to the line segregation is related to deviations in the field evaporation behavior at the facet junctions, compromising the lateral resolution of the atom probe reconstruction [31]. A set of lattice planes in the vicinity of the GB is resolved in the APT data for both adjacent grains, which reproduces the shape of the faceted interface; see Figs. 1(c) and 1(d). The atomic structure resolved by HAADF-STEM of the very same GB junction is illustrated in Fig. 1(d). The structural units of the GB are retained nearly completely up to the facet junction in both cases and the main difference arises in the core structures of the two types of junctions (Fig. S2 [21]). Strain sensitive STEM imaging (Fig. S3 [21]) indicates an increased strain at facet junction (II) suggesting that the local atomic reconstruction at the facet junction core play a decisive role in this segregation phenomenon.

This asymmetric line segregation was also studied at faceted $\sum 3$ grain boundaries with $\langle 110 \rangle$ tilt axis, since they are the most common grain boundary type present. The STEM and APT specimens were prepared in a single process to ensure that the distance between the probed areas remains in the range of a few μm to maintain similar atomic interface structure [26]. The specimens contain two grains separated by a faceted $\sum 3$ tilt GB perpendicular to the main specimen axis. The high detection efficiency of the LEAP 5000 APT microscope enables us to detect trace impurities in the range of 30 ppm for the interface region which translates to only 2 ppm for the probed sample volume. It is worth mentioning that the macroscopic description using a specific $\sum$ grain boundary type, is not describing the atomic arrangement at a local scale. Still, for simplicity and comparison with literature we use the wording of a faceted $\sum$ grain boundary.

First, the atomic structure of a faceted $\sum 3$ interface was characterized by HAADF-STEM as illustrated in Fig. 2. The main part of the GB is composed of two types of facets; the shorter segments are coherent $\sum 3\{111\}$ facets, whereas the longer segments are incoherent $\sum 3$ facets with a GB plane close to $\{112\}$, as seen in Fig. 2. The contrast in the corresponding low angle annular dark-field (LAADF) STEM micrograph in Fig. 2(b) visualizes the strain state present at the interface [32]. Strikingly, and at first glance unexpectedly, the strain state is not symmetrical at the two ends of the facets. Figure 2(c) gives a detailed view of the atomic motifs at the asymmetric $\{112\}$ facet and the core structures of the facet junctions. The structural units of the

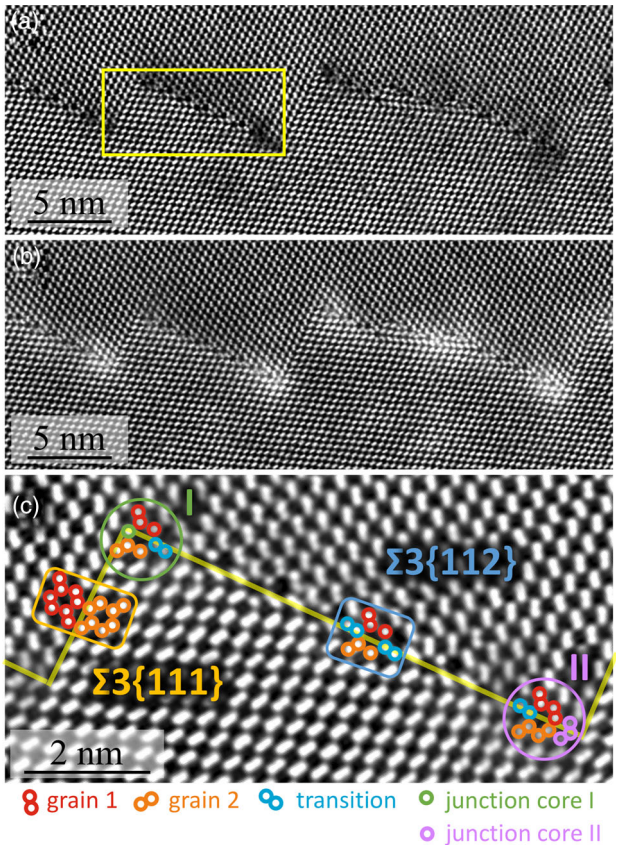

FIG. 2. Atomic structure of a faceted $\sum 3$ tilt grain boundary resolved by HR-STEM. (a) HAADF-STEM image of a TEM specimen resolving the faceted structure of the grain boundary. (b) Strain sensitive LAADF-STEM micrograph of the same area. (c) High resolution HAADF-STEM image of the GB segment highlighted in (a), resolving the structural motifs of the two facets and the facet junction cores (I) and (II).

GB planes correspond to those described in literature [33,34]. The length of both facets varies along the GB in the range of 5–40 nm and the trace of the global GB plane describes a slight curvature (Fig. S4 [21]). The incoherent {112} segments adopt an asymmetric reconstruction as seen in the slight rotation of the blue colored Si dumbbells. This is induced by finite size effects leading to a lateral displacement of the {111} planes (Fig. S5 and S6 [21]) [35]. This offset of lattice planes is of a general nature and also observed at faceted metallic grain boundaries and originates from a competition between the energy cost associated with the plane offsets and elastic contributions favoring straight lattice planes [14,36]. Similar to the $\sum 9$ interface, two different types of linear junctions exist, referred to as (I) and (II), respectively, as shown in Fig. 2(c). Junction (I) and the structural unit of $\sum 3\{112\}$ are nearly identical, only one of the blue colored Si dumbbells is replaced by a single atomic column. In contrast, the $\sum 3\{112\}$ motif is not retained in junction (II) and the atomic columns are densely packed, thus indicating the localization of compressive strain.

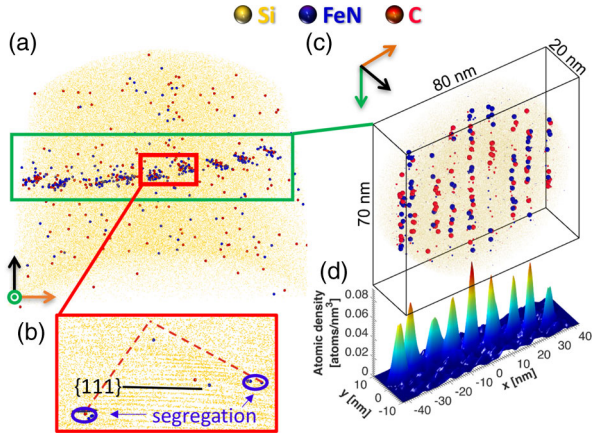

FIG. 3. Asymmetric line segregation observed by atom probe tomography at a faceted $\sum 3$ tilt grain boundary. (a) 3D atom map of the faceted interface viewed along the common tilt direction [110] showing co-segregation of C, Fe, and N impurities. Fe and N have been identified with the help of a FeN^{2+} molecular species. (b) Lattice planes can be resolved in the magnified volume. (c) 3D atom map of the grain boundary region, where the impurity atoms are plotted thicker in close proximity to the center of the segregation line for better visualization. (d) Corresponding atomic density plot resolving nine individual peaks.

The same linear segregation pattern is found for the faceted $\sum 3$ interface as seen by the atomic distributions in a needle-shaped specimen illustrated in Fig. 3. The volume in Fig. 3(a) is viewed along the common tilt axis of both grains. In this projection the GB is aligned "edge-on" and lattice planes are resolved in each grain [31], as illustrated in the magnified subvolume in Fig. 3(b). Within the GB region (green box), we reveal the preferential segregation of C, Fe, and N, in the form of nine lines, similar to those observed for the $\sum 9$ GB. The 3D impurity map in Fig. 3(c) shows that these segregation lines are almost parallel and extend through the entire reconstructed volume. The projected impurity density along the line axis is shown in Fig. 3(d), where nine peaks with a near-Gaussian shape are observed. The trace of the peaks describes a slight curvature following the overall curvature of the GB, and the distance among adjacent peaks is 8 ± 2 nm. The density profile of the middle segregation line has a slightly asymmetric full width at half maximum ($\omega_1 = 1.3$ nm, $\omega_1 = 1.6$ nm), which is likely related to the anisotropic spatial resolution of APT. 28 C^+ ions and 26 FeN^{2+} ions were detected within a volume of $10 \times 10 \times 80$ nm^3. With the knowledge of the one-to-one correlation described previously for the faceted $\sum 9$ GB, the arrangement and size of these lines strongly indicates that also here segregation is linked to the linear intersection of two grain boundary facets. Observation of the {111} planes in the APT reconstruction reveals that the segregation line is only located at facet junction (II) [Fig. 3(b)]. The separation distance of the linear intersections as determined by APT

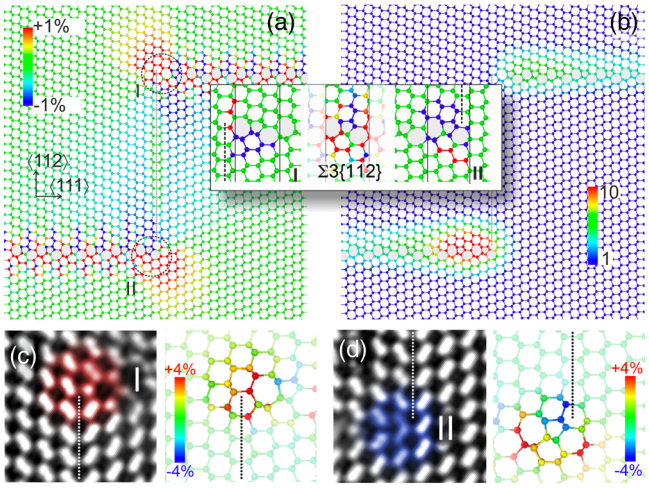

FIG. 4. MEAM potential simulations of the complex strain state and its impact on the C segregation at a faceted $\sum 3$ tilt grain boundary. (a) Local atomic strain at a nanoscale $\sum 3\{111\}$ twin segment embedded between two asymmetric $\sum 3\{112\}$ facets. Blue regions are under compressive, red regions under tensile strain. (b) C concentration with respect to the bulk. Inset middle: Atomic strain at a flat asymmetric, incoherent $\sum 3\{112\}$ segment. Color code is the same as in (a). Inset left and right: Atomic geometries at the junctions (I) and (II), respectively, with blue (red) $> 1\%$ ($< -1\%$) atomic strain than at the symmetry equivalent site at a flat asymmetric $\sum 3\{112\}$ segment. Vertical solid lines enclose the 1×1 unit cell of the asymmetric $\sum 3\{112\}$ GB. Dashed lines indicate the $\sum 3\{111\}$ twin. (c) Comparison of experimental STEM image and corresponding atomic strain at the core of facet junction (I). (d) Same comparison of facet junction core (II). The colored regions in the experimental images highlight the facet junction cores, respectively.

of 8 ± 2 nm is in excellent agreement with measurements from the STEM images of Fig. 2 ranging between 8 and 13 nm.

The atomistic origins and junction core effects of this asymmetric line segregation are explored by atomistic calculations employing a MEAM potential as shown in Fig. 4. The faceted grain boundary (Fig. 4) represents the lowest energy configuration for this dissociated interface and the incoherent $\sum 3\{112\}$ facets adopt an asymmetric reconstruction similar to that observed in the HAADF-STEM images of Fig. 2. The complex atomic strain state at the faceted grain boundary is illustrated in Fig. 4(a), where regions colored in red are under tensile strain and in blue under compressive strain, respectively. The distribution of compressive and tensile regions along the incoherent $\sum 3\{112\}$ facets is in agreement with calculations obtained for a similar, planar $\sum 3\{112\}$ interface [37]. The C concentration, integrated in a cylindrical region with 0.5 nm FWHM, at the faceted interface with respect to the average concentration in the bulk (c_0) at 300 K is shown in Fig. 4(b). Interestingly, the highest relative C concentration is found in the vicinity of facet junction (II) and is a factor of 10 times higher with respect to the bulk and more than twice as high as for facet junction (I). This asymmetric C distribution is in excellent agreement with experimental results and is attributed to the core structure and strain of the facet junctions, as can be seen in the inset of Figs. 4(a) and 4(b). In Figs. 4(c) and 4(d), experimentally obtained core structures of facet junction (I) and (II) are contrasted with the atomic strain determined from simulations. In facet junction (I), the majority of Si atoms in the junction core are under tensile strain [Fig. 4(c)], whereas in facet junction (II) the Si atoms are under largest compression [Fig. 4(d)]. This strain asymmetry at the facet junction cores originates from the disruption caused by the $\{111\}$ twin segment, leading to an amplification of compressive strains in facet junction (II), which in turn favors C segregation. Hence, the preferential segregation of C into the facet junction type (II) is directly connected to the underlying differences in junction core structure and the evolution of highest compressive strains. This observation also aligns with simulations of C segregation at different CSL GBs in Si, where it was found that the segregation free energy correlates with the hydrostatic pressure of all compressive sites within a GB [37].

The asymmetric segregation of Fe to facet junction (II) can be rationalized in terms of local bonding of interstitial Fe atoms to regions with strongly distorted Si bonds [38–40]. In similar grain boundary structures, it is found that the most preferable binding sites for Fe are fivefold coordinated Si atoms [38]. These configurations exhibit the lowest binding energies and are found in symmetric $\sum 3\{112\}$ segments, whereas bonding to the asymmetric $\{112\}$ interface is less preferred. Other observations suggest that interstitial Fe atoms also contribute to a strain relaxation that alters the spin energy of the local grain boundary defects [39]. Transferring these observations to the segregation of Fe to the present facet junction cores leads to the following conclusion: the Si triple column arrangement in the core of facet junction (II) [see Figs. 2(c) and 4(d)] provides preferred binding sites for Fe due to the presence of over-coordinated Si atoms. According to Ziebarth *et al.* [38], this promotes a nonspin polarized configuration of Fe and bond formation with neighboring Si atoms is possible. Along the facet junction core (II), every second Si atom is fivefold coordinated, which directly explains the obtained Fe atom density within the segregation lines [21]. This trapping of Fe impurity atoms into the facet junctions reduces their contribution to charge carrier recombination in the bulk and might have important implications on the electrical activity of mc-Si devices.

In conclusion, we observed a novel asymmetric segregation phenomenon at particular linear junctions of faceted GBs in mc-Si. By correlating atomic resolution HAADF-STEM with APT we resolved the atomic structure together with the local chemistry of the interfaces at the same specimen positions. The formation of segregation lines along facet junctions with highest compressive strain is

observed, following the faceted structure of the grain boundaries. Solute segregation to only one type of facet junction is rationalized by atomistic calculations. The local differences in atomic arrangements at the core structure of the facet junctions and the associated compressive strain, which is experimentally and theoretically resolved, are responsible for this novel segregation behavior. These findings go beyond the classical picture of planar McLean type segregation found in many bicrystal experiments and emphasize that the complex topology of interfaces in real materials plays a decisive role in the segregation behavior of interfaces. This, in turn, can have a tremendous effect on, e.g., the coarsening characteristics and transport properties of polycrystalline materials.

*Corresponding author.
liebscher@mpie.de

[1] M. P. Harmer, Science **332**, 182 (2011).
[2] G. Duscher, M. F. Chisholm, U. Alber, and M. Rühle, Nat. Mater. **3**, 621 (2004).
[3] J. P. Buban, K. Matsunaga, J. Chen, N. Shibata, W. Y. Ching, T. Yamamoto, and Y. Ikuhara, Science **311**, 212 (2006).
[4] Z. Wang, M. Saito, K. P. McKenna, L. Gu, S. Tsukimoto, A. L. Shluger, and Y. Ikuhara, Nature (London) **479**, 380 (2011).
[5] B. Feng, T. Yokoi, A. Kumamoto, M. Yoshiya, Y. Ikuhara, and N. Shibata, Nat. Commun. **7**, 11079 (2016).
[6] J. F. Nie, Y. M. Zhu, J. Z. Liu, and X. Y. Fang, Science **340**, 957 (2013).
[7] M. P. Seah, Acta Metall. **28**, 955 (1980).
[8] M. Guttmann, Metall. Trans. A **8**, 1383 (1977).
[9] P. R. Cantwell, M. Tang, S. J. Dillon, J. Luo, G. S. Rohrer, and M. P. Harmer, Acta Mater. **62**, 1 (2014).
[10] T. Frolov, D. L. Olmsted, M. Asta, and Y. Mishin, Nat. Commun. **4**, 1899 (2013).
[11] J. Luo, H. Cheng, K. M. Asl, C. J. Kiely, and M. P. Harmer, Science **333**, 1730 (2011).
[12] W. D. Kaplan, D. Chatain, P. Wynblatt, and W. C. Carter, J. Mater. Sci. **48**, 5681 (2013).
[13] A. Kwiatkowski da Silva, D. Ponge, Z. Peng, G. Inden, Y. Lu, A. Breen, B. Gault, and D. Raabe, Nat. Commun. **9**, 1137 (2018).
[14] E. A. Marquis, J. C. Hamilton, D. L. Medlin, and F. Léonard, Phys. Rev. Lett. **93**, 156101 (2004).
[15] A. Stoffers, B. Ziebarth, J. Barthel, O. Cojocaru-Mirédin, C. Elsässer, and D. Raabe, Phys. Rev. Lett. **115**, 235502 (2015).
[16] D. L. Medlin, K. Hattar, J. A. Zimmerman, F. Abdeljawad, and S. M. Foiles, Acta Mater. **124**, 383 (2017).
[17] K. J. Morrissey and C. B. Carter, J. Am. Ceram. Soc. **67**, 292 (1984).
[18] B.-K. Lee, S.-Y. Chung, and S.-J. L. Kang, Acta Mater. **48**, 1575 (2000).
[19] S. J. Dillon, M. Tang, W. C. Carter, and M. P. Harmer, Acta Mater. **55**, 6208 (2007).
[20] C. H. Liebscher, M. Yao, P. Dey, M. Lipi, B. Berkels, M. Herbig, J. Mayer, D. Raabe, G. Dehm, and C. Scheu, Phys. Rev. Mater. **2**, 023804 (2018).
[21] See Supplemental Material at http://link.aps.org/supplemental/10.1103/PhysRevLett.121.015702 for technical details on material characterization and atomistic simulations, which includes Refs. [22–25].
[22] K. Y. Xie, A. J. Breen, L. Yao, M. P. Moody, B. Gault, J. M. Cairney, and S. P. Ringer, Ultramicroscopy **112**, 32 (2012).
[23] F. Durand and J. C. Duby, J. Phase Equilib. **20**, 61 (1999).
[24] J. D. Struthers, J. Appl. Phys. **27**, 1560 (1956).
[25] M. I. Baskes, Phys. Rev. B **46**, 2727 (1992).
[26] A. Stoffers, O. Cojocaru-Mirédin, W. Seifert, S. Zaefferer, S. Riepe, and D. Raabe, Prog. Photovoltaics **23**, 1742 (2015).
[27] Y. Ohno, K. Kutsukake, M. Deura, I. Yonenaga, Y. Shimizu, N. Ebisawa, K. Inoue, Y. Nagai, H. Yoshida, and S. Takeda, Appl. Phys. Lett. **109**, 142105 (2016).
[28] Y. Ohno, K. Inoue, K. Fujiwara, K. Ujiwara, K. Kutsukake, K. Utsukake, M. Deura, I. Yonenaga, N. Ebisawa, Y. Shimizu, K. Inoue, Y. Nagai, H. Yoshida, S. Takeda, S. Tanaka, and M. Kohyama, J. Microsc. **268**, 230 (2017).
[29] A. Garg, W. A. T. Clark, and J. P. Hirth, Philos. Mag. A **59**, 479 (1989).
[30] B. Gault, M. P. Moody, J. M. Cairney, and S. P. Ringer, Mater. Today **15**, 378 (2012).
[31] B. Gault, M. P. Moody, J. M. Cairney, and S. P. Ringer, *Springer Series in Materials Science* (Springer, New York, 2012), Vol. 160.
[32] P. J. Phillips, M. D. Graef, L. Kovarik, A. Agrawal, W. Windl, and M. J. Mills, Ultramicroscopy **116**, 47 (2012).
[33] C. Fontaine, Appl. Phys. Lett. **40**, 153 (1982).
[34] H. Sawada, H. Ichinose, and M. Kohyama, J. Electron Microsc. **51**, 353 (2002).
[35] N. Sakaguchi, H. Ichinose, and S. Watanabe, Mater. Trans., JIM **48**, 2585 (2007).
[36] G. Dehm, B. J. Inkson, and T. Wagner, Acta Mater. **50**, 5021 (2002).
[37] P. Käshammer and T. Sinno, J. Appl. Phys. **118**, 095301 (2015).
[38] B. Ziebarth, M. Mrovec, C. Elsässer, and P. Gumbsch, Phys. Rev. B **91**, 035309 (2015).
[39] O. A. Al-Ani, J. Goss, N. Cowern, P. R. Briddon, M. Al-Hadidi, R. Al-Hamadany, and M. Rayson, Solid State Phenom. **242**, 224 (2015).
[40] O. A. Al-Ani, J. P. Goss, M. Al-Hadidi, P. R. Briddon, M. J. Rayson, and N. E. Cowern, J. Cryst. Growth **468**, 448 (2017).